IEEE Open Journal of Intelligent Transportation Systems

Received 14 July 2025; revised 31 October 2025 and 9 February 2026; accepted 21 March 2026.
Date of publication 31 March 2026; date of current version 3 April 2026.

Digital Object Identifier 10.1109/OJITS.2026.3679321

Mobile Laser Scanning for Road Pavement Distress Detection

AIMAD EL ISSAOUI[1], ZIYI FENG[1], MATTI LEHTOMÄKI[1], JOSEF TAHER[1], HARRI KAARTINEN[1,2], ANTERO KUKKO[1,3], DANIEL STEIGER[4], ALEXANDER REITERER[4,5], HANNU HYYPPÄ[3], AND JUHA HYYPPÄ[1,2,3]

[1]Department of Remote Sensing and Photogrammetry, Finnish Geospatial Research Institute (FGI), National Land Survey of Finland, 02150 Espoo, Finland
[2]Solid Potato Oy, 02230 Espoo, Finland
[3]Department of Built Environment, School of Engineering, Aalto University, 00076 Aalto, Finland
[4]Fraunhofer Institute for Physical Measurement Techniques IPM, 79110 Freiburg im Breisgau, Germany
[5]Department of Sustainable Systems Engineering, University of Freiburg, 79110 Freiburg im Breisgau, Germany

CORRESPONDING AUTHOR: A. EL ISSAOUI (aimad.elissaoui@maanmittauslaitos.fi)

This work was supported in part by the Research Council of Finland through grants "Towards Automatic Road Inspection" under Grant 365583 and "Innovative Methods for Measuring and Modelling the Dynamic Forest Road Quality" under Grant 362928; in part by European Regional Development Fund and Uudenmaan liitto through grant "Itseajavat autot ja tulevaisuuden data" under Grant R-00522; in part by European Union (EU) Agency for the Space Program Horizon 2020 Project "Galileo/GNSS-based Autonomous Mobile Mapping System (GAMMS)" under Grant 101004255; in part by the Research Council of Finland grant "Forest-Human-Machine Interplay—Building Resilience, Redefining Value Networks and Enabling Meaningful Experiences" under Grant 359175; and in part by the Henry Ford Foundation under Grant 20240081 and Grant 20230088.

ABSTRACT This study investigates the efficacy of Mobile Laser Scanning (MLS) for detecting pavement distresses from precise 3D point cloud data. A conventional MLS system was evaluated against a high-accuracy pavement mapping reference system. The study data were collected by a Roamer-R4DW mobile mapping system equipped with a Riegl VUX-1HA scanner, while the reference data were acquired using a Fraunhofer PPS-plus-based mobile mapping system (PPS-plus), which maps road surfaces at sub-millimeter level. A novel automatic distress detection algorithm was developed, improving upon previous methods to significantly enhance accuracy. For algorithm validation, nine 10-meter-long pavement sections were annotated using PPS-plus data to serve as ground truth. The algorithm achieved an $\boldsymbol{F_1}$ score of 0.87 for detecting distresses wider than 2 cm. The same algorithm was applied to Roamer-R4DW and compared to the manual reference, resulting in an $\boldsymbol{F_1}$ score of 0.77. To assess the generalizability of the previous findings, the evaluation was expanded to a 3.2-km-long road section. Utilizing algorithm-generated reference from PPS-plus data, the automatic distress detection algorithm resulted in an $\boldsymbol{F_1}$ score of 0.66 for the Roamer-R4DW data. Additionally, this study addressed a critical research gap: the lack of distress volume and area assessments using MLS data. We achieved coefficients of determination of 0.93 and 0.77 for distress volume and area respectively for the same 3.2-km-long road section. The results of this study underscore the potential of conventional MLS systems, such as the Roamer-R4DW, for surveying and mapping pavement and road environments in 3D. Representative dataset: https://doi.org/10.5281/zenodo.19267189.

INDEX TERMS Crack, mobile laser scanning, pavement distress detection, point cloud, pothole, road, rut.

I. INTRODUCTION

MAINTAINING roads is essential for transportation safety and efficiency. Reliable transport systems support both economic growth and societal well-being. The road maintenance and repair planning require an accurate assessment of pavement condition, which is often determined by the degree of pavement distresses. Pavement distresses, such as cracks, potholes and rutting, often indicate problems in the deeper road structure. Additionally, they allow water to penetrate the road surface, further deteriorating the road structure. Meanwhile, the uneven surface and accumulated water on rainy days also pose hidden dangers to driving safety. Therefore, early detection of pavement distress is essential to prevent costly repairs, accidents, and traffic jams caused by deteriorating roads.

Roads can deteriorate due to a variety of factors, including improper maintenance, unsuitable construction materials,

The review of this article was arranged by Associate Editor Abel C. H. Chen.

excess traffic loads, poor surface drainage, and challenging climatic conditions [1], [2], [3], [4]. Diverse root causes result in a variety of internal and superficial damage on the road network, which also challenges the methods proposed for measuring, analyzing, and reporting the condition of pavement.

Research on pavement distress detection using remote sensing techniques has commonly employed two-dimensional (2D) image intensity algorithms due to their versatility and cost-effectiveness [5]. However, those methods encounter difficulties with deriving depth information, uncertain detection in varying lighting conditions, and misidentification of non-crack features [6]. Despite improvements through applying advanced computational and AI methods, selecting an appropriate set of parameters remains a challenge due to variability in crack characteristics across diverse pavement compositions and image quality concerns (e.g., motion, illumination, and object shadows, pavement and gravel mixture, and presence of road paint, patches and repairs). Methods utilizing 2D image processing also often neglect vital geometric information, revealing limitations in comprehensively detecting pavement cracks [4], [7], [8], [9], [10], [11], [12], [13], [14].

Photogrammetry and laser scanning represent two prominent approaches for three-dimensional (3D) reconstruction of road surface and detection of surface defects such as cracks, potholes and depressions. Photogrammetry relies on image sequences to build 3D models. However, it is sensitive to environmental factors and demands a large number of images [15]. Crack detection using 3D information from photogrammetric techniques, e.g. structure from motion, enables automated analysis of large datasets by representing road surfaces as 3D point clouds [16], [17], [18]. In contrast, laser-based techniques offer a more resilient approach, which is less impacted by lighting conditions and provides richer information [19]. Laser scanning has gained popularity in civil engineering with several studies confirming the effectiveness of the Terrestrial Laser Scanning (TLS) technique in identifying pavement surface distress [20], [21], [22]. Numerous studies and reviews on crack detection using laser-based techniques have been published in recent years [23], [24], [25], [26], [27], [28], [29], [30].

Mobile Laser Scanning (MLS) systems are increasingly used for detecting road features and identifying pavement distress. Feng et al. proposed a semi-supervised point-level method using graph convolutional networks (GCN) to detect cracks from MLS data collected on the Qinghai-Tibet Highway [31]. Yan et al. [32] utilized a scan line method to extract road points from a point cloud. The method combined the identified seed road points from scan lines and a moving least square line fitting algorithm to determine the full set of road points for each scan line. Zhong et al. transformed MLS point clouds into a regular grid structure and utilized image-based methods to detect three types of pavement cracks on 220-m-long road sections, achieving high F_1 scores for the detected crack curves [33]. El Issaoui et al. used an MLS system for rut detection and depth estimation, applying a low-pass filter to the individual profiles and verifying the results with TLS [21]. Del Río-Barral et al. employed a low-pass filter to preliminarily identify crack points, further refined through manual validation using images [28]. More recently, del Río-Barral et al. developed a machine-learning-based approach, utilizing geometric features of MLS point clouds derived through principal component analysis [34]. In contrast, Guo et al. integrated vehicle-mounted panoramic imagery with MLS data, using convolutional neural networks for initial crack detection and subsequently refining crack geometry through point cloud-based elevation analysis [35]. Study by Xia et al. employed an MLS system using a RIEGL VUX-1HA scanner to detect pavement subsidence deeper than 1.5 cm by analyzing elevation deviations along a 100-meter test section [36]. Similarly, Pascucci et al. explored point-wise crack classification using MLS data, where both the detection and the manually annotated reference labels were derived from the same point cloud, demonstrating high accuracy for identifying longitudinal and transverse cracks across 27 targeted segments [37].

As described above, previous laser studies have demonstrated the feasibility of crack detection in pavements. However, many of these studies are constrained by limited test areas, hindering analysis of extensive road sections and use of high-accuracy reference data. In some cases, both the detection results and the reference annotations are derived from the same point cloud data. While this simplifies the workflow, it undermines the reliability of performance evaluation, particularly when the data originate from conventional MLS systems that lack the resolution and ranging accuracy required for generating high-quality ground truth. Although they have demonstrated novel work, more in-depth quantitative evaluations for distress detection are needed. Additionally, assessments of distress volume and area have been lacking. This study directly addresses these limitations by conducting a comprehensive analysis of pavement distress detection using MLS. We analyzed a 3.2-km-long road section, including detailed volume and area calculations of distresses, and validated our findings with high-accuracy reference data. In addition, our research introduces a novel algorithm that merges and refines three previously developed algorithms, resulting in a substantial improvement in accuracy and enhancing the overall performance and robustness of distress detection.

II. RESEARCH DESIGN AND MATERIALS

A. RESEARCH APPROACH

The evaluation framework of this study was designed to assess both the algorithmic performance and the feasibility of conventional MLS systems for distress detection. The study design consists of three distinct validation stages, including algorithm validation, evaluation of conventional mobile mapping system and its generalizability on distress detection:

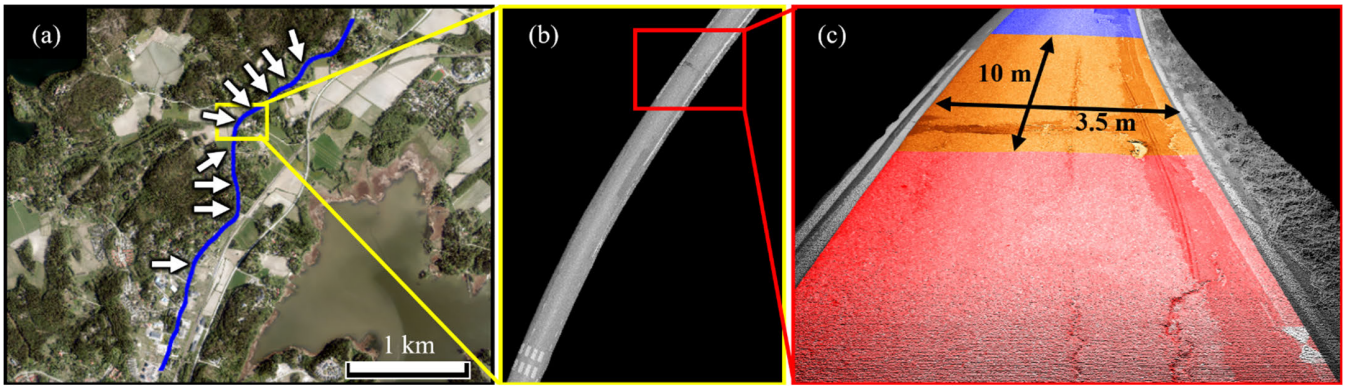

FIGURE 1. Study area and test section layout. (a) Aerial view of the 3.2-km survey area, with the trajectory marked in blue and the locations of the reference data validation sections marked by white arrows. (b) A zoomed-in point cloud visualization of the road segment highlighted by the yellow box in (a). (c) Visualization of the examined 10-meter test sections from the red box in (b), showing the reference data collected by the PPS-plus system, with sections colored by red, orange, and blue. The single painted line on the right side of the road surface marks the right edge of the lane, whereas the double line on the left side indicates the center line, which is between two opposing lanes.

- First, to isolate the performance of the proposed detection algorithm from hardware limitations, the algorithm was applied to high-density point cloud data acquired by a reference system. The results were validated against manually annotated ground truth from selected validation sections. This step established the baseline accuracy of the algorithm itself.
- Next, to assess the capability of the conventional MLS system on distress detection, the same algorithm was applied to the conventional MLS data. These results were compared against the same manually annotated ground truth used in the first stage.
- Finally, to evaluate the system's performance on a larger scale, the assessment was extended to a significantly longer road segment. For this stage, the reference data was generated automatically by applying the validated algorithm to the high-density reference point clouds. This allowed for a dense, kilometer-scale quantitative evaluation of the conventional MLS system under diverse road conditions but this approach is limited by the reference data accuracy.

B. DATA DESCRIPTION

MLS point cloud data was collected on a 3.2-km-long stretch of a two-lane regional road (road number 11311) in the municipality of Kirkkonummi, Finland (Fig. 1). Two MLS data sets were collected on the same day in 2019 using two MLS systems. The surveys were conducted at driving speeds corresponding to the speed limits of 40–50 km/h. On the day of the measurement, the road surface was dry, and the weather was partly cloudy. The road exhibits typical geometric variability of Finnish regional roads. The horizontal alignment includes straight segments connected by curves of varying curvature. The vertical profile is varying, with an elevation range of approximately 14 m over the segment. The longitudinal grade varies from near-flat sections to local slopes exceeding 7%. Additionally, the road features superelevation in curved sections, which introduces varying vehicle dynamics and scanning geometries.

The first dataset was collected using the PPS-plus, which produces extremely dense and accurate point clouds comparable to TLS. Due to its high point density and measurement accuracy, the PPS-plus dataset was used as a reference (hereinafter referred to as the reference data) for evaluating the Roamer system's performance. The second dataset was collected using the Roamer system, a conventional MLS system designed for road environment mapping, which has potential for operational pavement distress detection while simultaneously mapping the road environment.

PPS-plus is equipped with the Pavement Profile Scanner (PPS, Fraunhofer IPM, Germany), which utilizes phase-shift (PS) ranging technology, as well as an Applanix POS LV 420 system that integrates both an Inertial Measurement Unit (IMU) and a GNSS receiver to estimate the location and orientation of the system (Fig. 2(a)). The system is developed by the Fraunhofer Institute in particular for road surface mapping, and it is capable of measuring 800 cross-track profiles and one million points per second. The scanner was approximately 3 m above the road surface. The scanner's 70-degree field of view covered more than 4.5 meters in the cross-track direction, which was sufficient to fully capture the 3.5-meter-wide lane. In this way, the point cloud obtained from the road surface was very dense for the pavement distress detection. In our dataset, the number of points on one profile was over 900 and the distance between consecutive points within the profile varied between 3 and 5 mm, being denser right under the scanner and less dense towards the edges of the lane. The distance between consecutive profiles varied between 1.2 and 1.7 cm. The accuracy of the distance measurement of the scanner is better than 0.15 mm [38]. The performance of the PPS system has been independently evaluated by the Swedish National Road and Transport Research Institute (VTI) [39], which reported high agreement with reference measurements and a measurement repeatability

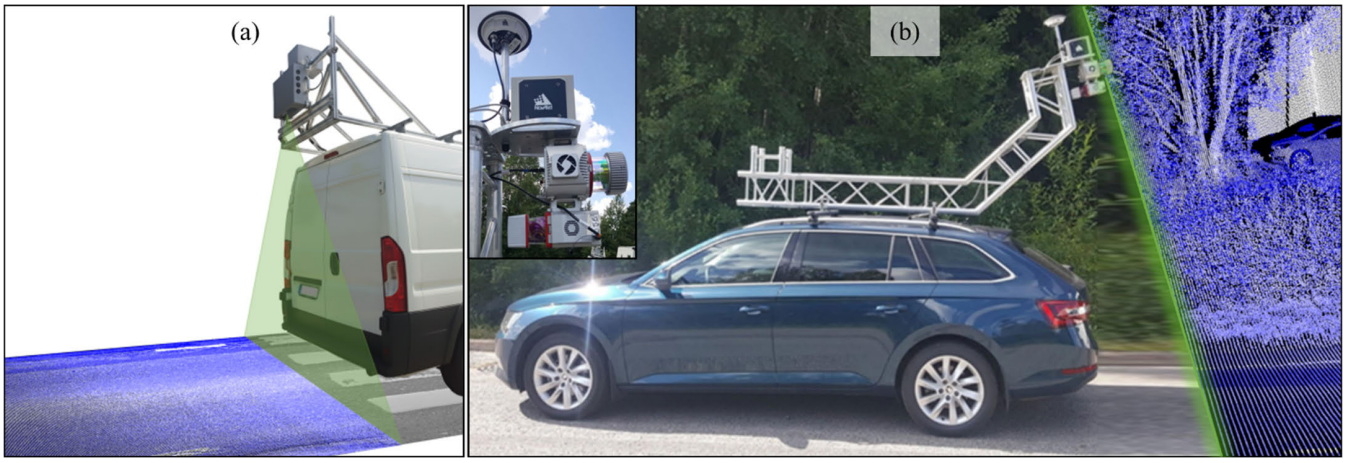

FIGURE 2. Fraunhofer PPS-plus reference system, illustrating its scan angle (green) and the resulting dense pavement point cloud (blue) on the road surface. (b) The Roamer-R4DW conventional MLS system, which captures the entire road environment with a 360-degree scanner (green line and blue point cloud), resulting in a comparatively sparser point cloud on the road surface; the inset provides a close-up of the sensor setup. (Fig. 2. (b) modified from [21], ©2021 by the authors. Licensed under CC BY 4.0).

of approximately 0.09 mm under controlled test conditions, confirming the system's capability for stable, sub-millimeter pavement surface profiling.

The conventional MLS data set to be studied was collected using the Roamer-R4DW mobile mapping system (Fig. 2(b)), developed at the Finnish Geospatial Research Institute (FGI). The system consists of a NovAtel ISA-100C IMU, a Pwrpak7 global navigation satellite system (GNSS) receiver and two laser scanners: the Riegl VUX-1HA and Riegl miniVUX-1UAV (Riegl GmbH, Austria). For the purpose of this study, only the Riegl VUX-1HA data was used (hereafter referred to as Roamer data). The Riegl VUX-1HA was located on the roof of the vehicle at a height of 2.9 m above the road surface and angled at approximately 15 degrees from the perpendicular to the road. Unlike the reference data, this scanner has a field of view of 360 degrees around one axis and thus collects data from the entire road environment when the platform is moving. The scanner was set to measure 250 profiles per second at a pulse repetition frequency of 1017 kHz. The distance between consecutive points in the Roamer data within the road surface cross-track profile of the lane varied between 4 and 6 mm, and the distance between profiles varied between 4 and 5 cm, depending on the driving speed. The measurement accuracy of the Riegl VUX-1HA (manufactured 2017) scanner was 5 mm with 3 mm precision. For a more detailed description of the Roamer-R4DW mobile mapping system, the reader is directed to [21].

C. DATA PREPROCESSING

The preprocessing of the data included three main steps: classifying lane points (identification of road points, lane markings, and lane points), noise removal, and registration. The lane classification started with the identification of road points in the Roamer data. Due to the limited field of view of the PPS, the reference data already contained points mainly from the driven lane and surrounding road surface. The next task was to identify the edges of the lane to extract the desired study area. In this work, the lane points were defined as points between the painted line markings located at the center and edge of the road. Once the painted lines were identified from the data, a spline was fitted to the extracted and often incomplete marking points to ensure continuity. The points between the fitted splines at the center and edge of the road were classified as lane points. Additionally, a 20 cm buffer zone extending outwards from the lane edge was included during the algorithmic processing. This buffer ensured that valid reference surfaces could be generated at the lane boundaries, preventing edge effects, although only distress points located within the actual lane limits were retained for the final analysis.

Transient objects above the road surface caused stray points lying in the air. The objects included small bits and loose gravel rocks, insects or trash that temporarily appeared above the pavement during the measurement. The stray points were removed by first applying a low-pass filter of order 25 to each profile across the lane. The resulting smoothed profile was then compared point by point with the original profile, and points with elevation change (the original elevation of the point minus that of the filtered profile) greater than 6 mm were considered to be above ground noise points and removed.

After classification and noise removal of the lane points, the Roamer data was registered with the corresponding reference data. Even though both data sets were directly geo-referenced using a dedicated positioning system, the position solutions of the two different systems were not coincident at all locations, and the two data sets had to be matched to each other. Since positioning accuracy was not constant over the measurement period, it was decided to split the data into 10 m driveway-oriented sections (Fig. 1(c)), corresponding to the previously defined test sections. Positioning accuracy was affected by several factors, such as the visibility of the satellites at the time of the measurement, which led to signal degradation. Registering the pavement surface point

clouds using only geometry and Iterative Closest Point (ICP) algorithm was challenging, especially in the horizontal plane, due to the planar nature of the road. Therefore, registration (rigid transformation) was performed using extracted road markings and automatically segmented large cracks and potholes. To quantify the accuracy of the co-registration, we utilized painted hourglass-shaped ground control signals located approximately every 50 meters along the road section, introduced in [22]. The final registration accuracy was evaluated by comparing the signal centers between the registered Roamer and reference datasets. This comparison resulted in a horizontal Root Mean Square Error (RMSE) of 2.3 cm and a systematic horizontal bias of less than 0.6 cm.

III. METHODS

A. DISTRESS DETECTION ALGORITHM

This study proposes a novel distress detection method that utilizes three algorithms developed in [22]. Our goal was to improve the accuracy of distress detection by identifying distress points that are consistently detected by multiple algorithms. In the development of the algorithm in this study, we utilized profile-based filtering, surface fitting, and local surface roughness algorithms described in detail in [22].

The profile-based filtering algorithm processes a pavement point cloud that is structured into transverse profiles. These profiles are individually filtered using a digital filter to generate ideal, distress-free surfaces. Longitudinal profiles are then constructed by grouping corresponding points from each transverse profile, such that the first longitudinal profile consists of the first point from every transverse profile, the second consists of the second point from each, and so on. These longitudinal profiles are also filtered using the same approach. In both cases, points that remain below the resulting ideal profiles are classified as distress points.

The surface fitting algorithm divides the test area into 50 cm by 50 cm windows and fits a polynomial surface within each window. Points that fall below the fitted surface are identified as distress indicators.

The local surface roughness algorithm estimates surface roughness value for each point, and extracts points as distress in area where surface is not smooth enough.

These three algorithms were selected as they were the top-performing methods identified in [22], each exhibiting sensitivity to different distress characteristics. The profile-based filtering algorithm excels at capturing distinct vertical deviations, such as potholes and transverse cracks, ensuring the detection of structural depth where texture-based methods may fail (e.g., at the smooth bottom of a wide depression). The surface fitting algorithm acts as a confirmation for local surface depressions, effectively validating deviations from the road plane. To complement these, the local surface roughness algorithm was included for its sensitivity to texture; it previously outperformed other methods on 'difficult' plots [22] characterized by complex or irregular distress patterns (e.g., disintegration), where clear geometric dips are less defined. By fusing these complementary approaches, the proposed strategy leverages the specific strengths of each to maximize detection robustness across varying distress types. Furthermore, they represent the three dominant classes of geometric detection methods found in the literature: scan-line profiling [28], [40], reference surface fitting [41], [42], and local geometric feature analysis [10], [34].

The determination of key parameters, such as the filter order, window size, neighborhood radius, and decision thresholds, was primarily based on the extensive comparative study in [22]. Minor adjustments were made solely based on domain expertise regarding the specific sensor characteristics; for instance, detection thresholds were aligned with the known ranging precision and point density of the PPS-plus and Roamer systems to prevent noise-induced false positives.

To improve the reliability of the distress detection, we propose a strategy that identifies distress points by intersecting the results of the three algorithms. We adopted this two-out-of-three voting rule to target a high F_1 score, which balances precision and recall by weighting false positives and false negatives equally. This method effectively filters out potential false positives by only retaining distress points detected by at least two algorithms. This data fusion workflow is visualized in the flowchart in Fig. 3. If letting A_1, A_2, and A_3 represent the sets of the 3D distress points detected by the profile-based, surface fitting, and surface roughness algorithms, respectively, the output P of our new algorithm can be expressed mathematically using equation:

$$P = (A_1 \cap A_2) \cup (A_1 \cap A_3) \cup (A_2 \cap A_3)\,. \tag{1}$$

B. VALIDATION OF THE DISTRESS DETECTION ALGORITHM USING PPS-PLUS REFERENCE DATA

We selected nine 10-meter validation sections of PPS-plus data to evaluate the accuracy of the developed distress detection algorithm. The validation sections were selected from different locations throughout a 3.2-kilometer study road on purpose to ensure representation of different types of distresses for a comprehensive evaluation. The locations of the selected validation sections are shown in Fig. 1(a) and span different longitudinal positions along the route, covering varying road geometries, slopes, and driving directions.

Reference data was manually annotated into distress and non-distress points for all cracks, potholes and other distress types using CloudCompare [43], based on visual inspection of elevation and intensity differences. All distresses wider than 1 cm were annotated. In addition, ruts deeper than 2 cm were considered a form of distress due to their severity and classified as distresses as well.

For distress detection algorithm validation, the nine validation sections in the PPS-plus data were also classified by the algorithm. We compared the distresses detected by the algorithm to the manually annotated distresses. By considering the manual annotation as ground truth, we calculated precision, recall, and F_1 score using the

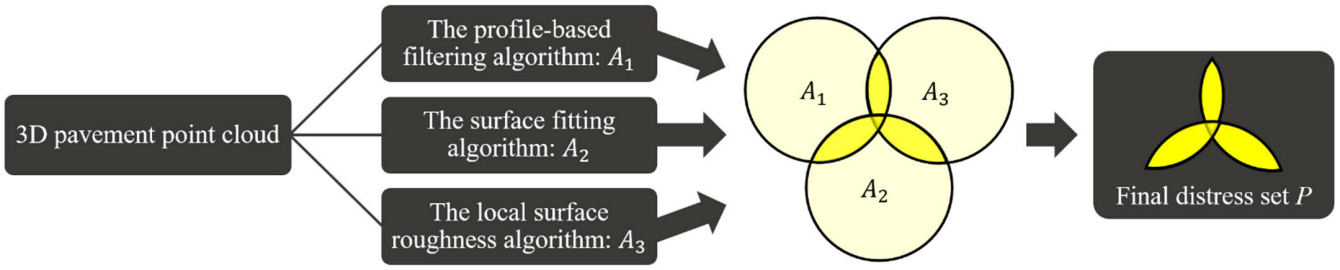

FIGURE 3. Flowchart of the proposed distress detection algorithm. The 3D pavement point cloud is processed in parallel by three algorithms derived from [22]. The final distress set *P* is generated by retaining only the points detected by at least two of the three algorithms, and it is visualized by the more saturated yellow areas in the Venn diagram.

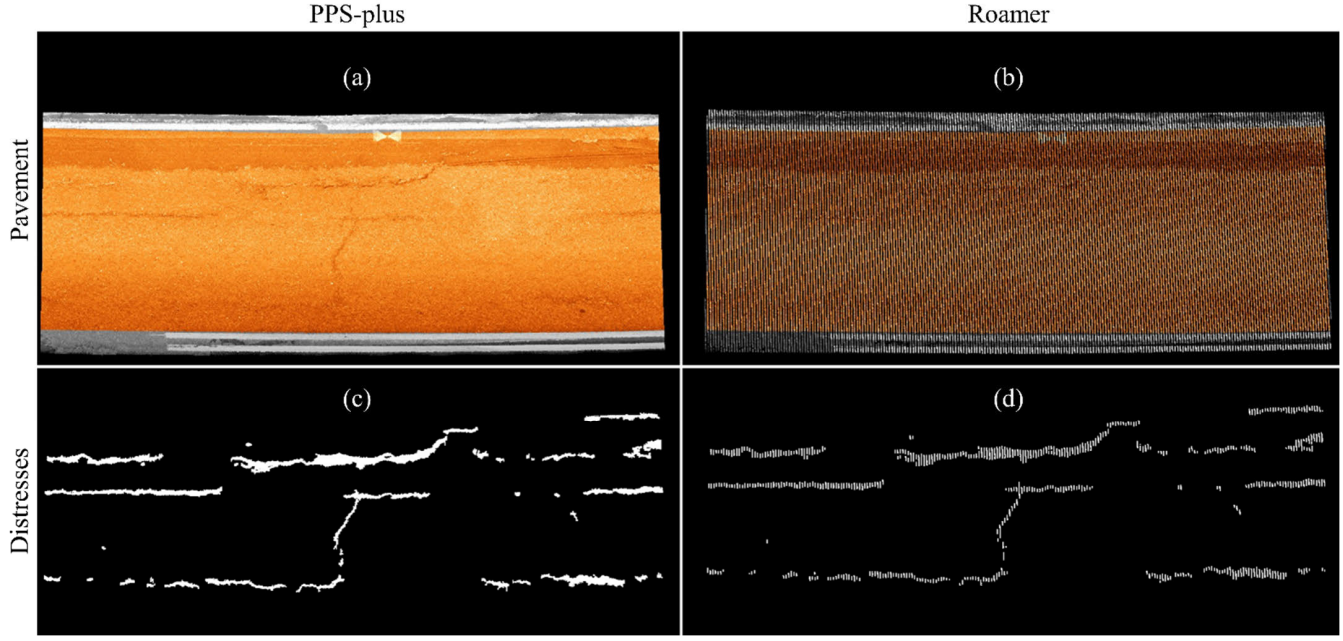

FIGURE 4. Comparison of reference and Roamer data for a 10-meter-long validation section. (a) Reference data, with the analyzed driving lane colored orange. (b) Corresponding Roamer data. (c) Manually classified ground truth distresses from the reference data. (d) Ground truth distresses projected onto the Roamer data.

following equations:

$$\text{Recall} = \frac{\text{TP}}{\text{TP} + \text{FN}}, \tag{2}$$

$$\text{Precision} = \frac{\text{TP}}{\text{TP} + \text{FP}}, \tag{3}$$

$$F_1 = 2 \cdot \frac{\text{Precision} \cdot \text{Recall}}{\text{Precision} + \text{Recall}}, \tag{4}$$

where TP (true positives) denotes the number of points correctly classified as distress, FP (false positives) denotes the number of points incorrectly classified as distress when they are actually non-distress, and FN (false negatives) denotes the number of distress points incorrectly classified as non-distress.

C. CONVENTIONAL ROAMER MLS SYSTEM EVALUATION FOR PAVEMENT DISTRESS DETECTION

To evaluate the capability of the conventional Roamer MLS system in distress detection, we applied the distress detection algorithm validated in Section III-B to the point cloud data acquired by the Roamer system. The same nine validation sections, ground truth labels, and evaluation metrics from Section III-B were used. Due to the distance between consecutive profiles in the Roamer system, the evaluation focused on distresses wider than 2 cm. Because the profile spacing differed between the reference and Roamer data, the manually classified ground truth was projected onto the Roamer point cloud. Fig. 4(a) shows a 10-meter-long validation section from PPS-plus data and Fig. 4(b) the corresponding Roamer data. Fig. 4(c) shows the manually classified reference data, and Fig. 4(d) presents the projected data.

To assess the generalizability of the Roamer system's accuracy in pavement distress detection, the study was expanded to the entire 3.2-kilometer road section (322 test sections). On this road section, the distresses were detected by the algorithm from the PPS-plus data to create a large ground truth dataset of distresses with a known margin of error. The distresses detected from the Roamer data by the algorithm

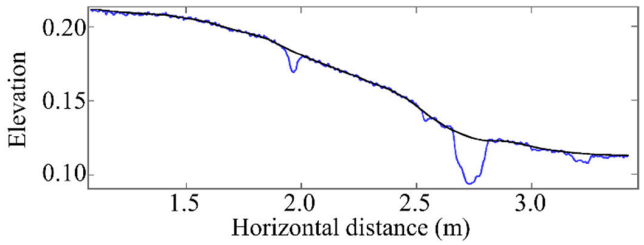

FIGURE 5. Cross-sectional profile of the road surface (blue) vs. the reconstruction of ideal profile (black). The dips in the blue line indicate surface distresses, such as cracks or potholes. The ideal profile smooths out these anomalies, serving as a reference to quantify distress depth and volume.

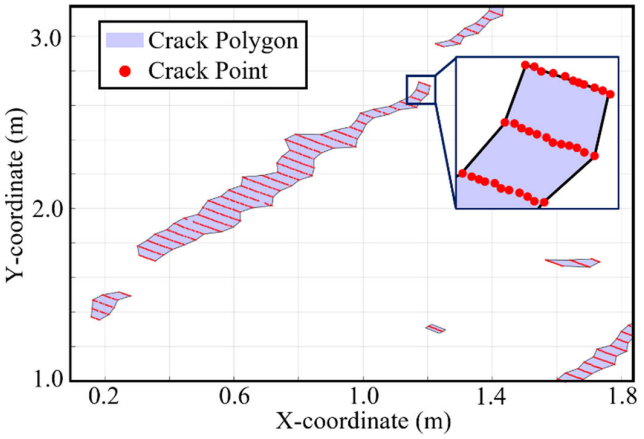

FIGURE 6. Visualization of detected crack points and corresponding crack polygons. The inset provides a magnified view, clearly illustrating the relationship between the individual crack points and the constructed polygon.

were compared to this large ground truth dataset for a broad comparative analysis. This comprehensive evaluation was necessary to ensure that the initial findings, based on a limited number of validation sections presented earlier in this study, could be generalized to a larger and more diverse dataset. By doing so, the robustness and reliability of both the distress detection algorithm and the Roamer system were thoroughly assessed.

D. DISTRESS VOLUME AND AREA CALCULATION

For assessing the severity of pavement distress, the volume and area of detected distresses were calculated. The volume calculation is based on the reconstruction of an ideal pavement surface without distresses. On the other hand, the area parameter calculation is based on the formation of distress polygons.

The distress volume calculation method utilized the profile filtering method proposed by [21], but with specific modifications, to reconstruct an ideal pavement surface unaffected by distresses. The modifications mainly involved multiple iterations using varying filter orders after which an ideal profile without distress was reconstructed, as shown in Fig. 5. To determine the distress depth, we measured the distance from each distress point to this ideal surface. The distress points were then resampled to maintain uniform distance, allowing us to compute the volume. This calculation relied on three following parameters: the distance between the distress point and the ideal surface (depth), the distance to the neighboring distress point (width), and the distance to the neighboring profile (length). The volume of each distress was obtained by summing the volumes of the corresponding cuboids, and the total distress volume for the entire plot was derived by combining all individual distress volumes.

In the distress area calculation method, the detected distress points were clustered based on the proximity across neighboring scan profiles, with each resulting cluster representing a single distress object. The surface area of a distress object was defined as the area of the polygon formed by connecting the outermost points of each profile inside the cluster. In cases where a distress appeared in only a single profile with no corresponding detection in neighboring profiles, its area was estimated by multiplying its length along the profile by the spacing between profiles. Fig. 6 shows identified distress points in red and the polygons created by the algorithm for area calculation.

In this study, the accuracies of the volume and area calculations were evaluated using the following metrics: Coefficient of Determination (R^2), Correlation, Root Mean Square Error (RMSE), Mean Absolute Error (MAE) and Bias. Assuming the estimated values are denoted by $\hat{y}_i$, the reference values by y_i, the mean of the reference values by $\bar{y}$, the mean of the estimated values by $\bar{\hat{y}}$, and the index of each section by i, the formulas for the accuracy metrics are as follows:

$$R^2 = 1 - \frac{\sum_{i=1}^{n} \left(y_i - \hat{y}_i\right)^2}{\sum_{i=1}^{n} \left(y_i - \bar{y}\right)^2}, \tag{5}$$

$$\text{Correlation} = \frac{\sum_{i=1}^{n} \left(y_i - \bar{y}\right)\left(\hat{y}_i - \bar{\hat{y}}\right)}{\sqrt{\sum_{i=1}^{n} \left(y_i - \bar{y}\right)^2} \cdot \sqrt{\sum_{i=1}^{n} \left(\hat{y}_i - \bar{\hat{y}}\right)^2}}, \tag{6}$$

$$\text{RMSE} = \sqrt{\frac{1}{n} \sum_{i=1}^{n} \left(\hat{y}_i - y_i\right)^2}, \tag{7}$$

$$\text{MAE} = \frac{1}{n} \sum_{i=1}^{n} \left|\hat{y}_i - y_i\right|, \tag{8}$$

$$\text{Bias} = \frac{1}{n} \sum_{i=1}^{n} \left(\hat{y}_i - y_i\right), \tag{9}$$

IV. RESULTS AND DISCUSSION

A. RESULTS OF THE ALGORITHM VALIDATION USING PPS-PLUS DATA

When applied to the point cloud data acquired by the reference system (PPS-plus), the integrated distress detection algorithm achieved a total recall of 0.87, precision of 0.87, and F_1 score of 0.87 for the distresses wider than 2 cm, indicating a high degree of accuracy in correctly identifying distress points. The 2 cm threshold was selected to match the detection capabilities of the Roamer MLS system, which, due to its lower profile density, cannot reliably capture

TABLE 1. Validation results for the distress detection algorithm based on the nine 10-meter validation sections from the PPS-plus reference dataset. algorithm-detected points in distresses wider than 2 cm are compared to manually classified ground truth, as described in section III-B.

Section ID	TP	FP	FN	Recall	Precision	F_1 score
1	1991	405	417	0.83	0.83	0.83
2	12707	3742	1785	0.88	0.77	0.82
3	14918	1477	1511	0.91	0.91	0.91
4	7462	1404	956	0.89	0.84	0.86
5	7170	979	852	0.89	0.88	0.89
6	1046	223	333	0.76	0.82	0.79
7	2276	391	1143	0.67	0.85	0.75
8	14190	927	1746	0.89	0.94	0.91
9	5234	782	1395	0.79	0.87	0.83
TOTAL	**66994**	**10330**	**10138**	**0.87**	**0.87**	**0.87**

TABLE 2. Validation results for the distress detection algorithm based on the nine 10-meter validation sections from the PPS-plus reference dataset. algorithm-detected points in distresses wider than 1 cm are compared to manually classified ground truth, as described in section III-B.

Section ID	TP	FP	FN	Recall	Precision	F_1 score
1	2329	479	662	0.78	0.83	0.80
2	12927	3802	1778	0.88	0.77	0.82
3	15086	1637	1496	0.91	0.90	0.91
4	7900	1454	1378	0.85	0.84	0.85
5	7742	980	1062	0.88	0.89	0.88
6	1293	229	729	0.64	0.85	0.73
7	2753	363	2448	0.53	0.88	0.66
8	14619	864	2876	0.84	0.94	0.89
9	5816	734	2109	0.73	0.89	0.80
TOTAL	**70465**	**10542**	**14538**	**0.83**	**0.87**	**0.85**

smaller-scale surface variations. The results in detail are shown in Table 1.

To further evaluate the algorithm's performance in higher-resolution conditions, we also assessed the algorithm's potential to detect smaller-scale distresses. This evaluation considered all distresses wider than 1 cm. As summarized in Table 2, this test resulted in a recall of 0.83, a precision of 0.87, and an F_1 score of 0.85. These results demonstrate the algorithm's capability to detect finer-scale distresses with high precision.

To assess the specific contribution of the fusion strategy, the performance of the integrated algorithm was compared against the three base algorithms individually on the same validation dataset. The individual algorithms exhibited distinct limitations. The surface fitting and surface roughness algorithms achieved high recall rates (0.88 and 0.87, respectively) but suffered from low precision (0.63 and 0.68), indicating a susceptibility to false positives caused by surface texture anomalies. In contrast, the profile-based filtering algorithm demonstrated high precision (0.94) but a significantly lower recall (0.62).

As noted earlier (Table 1), the proposed fusion strategy achieved an F_1 score of 0.87, outperforming the best individual method (surface roughness, $F_1 = 0.76$) by approximately 14%. This improvement demonstrates that the voting strategy effectively mitigates the false positives inherent to the surface-based methods while preserving their ability to detect distresses missed by the profile-based filtering approach.

B. RESULTS OF THE CONVENTIONAL ROAMER MLS SYSTEM EVALUATION

The Roamer system demonstrated respectable performance in distress detection but showed slightly lower accuracy metrics compared to the PPS-plus results reported in Section IV-A. This difference is primarily due to the Roamer system's lower ranging accuracy and scan frequency, which result in lower point density. The accuracy of the Roamer system in distress detection was evaluated as described in Section III-C. For pavement distresses wider than 2 cm, the recall, precision, and F_1 score of distress detection from Roamer data were 0.76, 0.77, and 0.77, respectively (Table 3). Despite the lower ranging accuracy and scan frequency, the algorithm maintained reliable performance, indicating its practical suitability for pavement distress mapping using conventional MLS systems under field conditions.

To test the generalizability of the distress detection algorithm applied to Roamer system data, we evaluated 322 test sections against a reference generated using the procedure described in Section III-C. In this larger-scale

TABLE 3. Evaluation results for the distress detection algorithm based on the nine 10-meter validation sections from the roamer dataset. algorithm-detected points in distresses wider than 2 cm are compared to projected ground truth labels derived from the PPS-plus reference dataset, as described in section III-C.

Section ID	TP	FP	FN	Recall	Precision	F_1 score
1	308	42	233	0.57	0.88	0.69
2	2747	1810	633	0.81	0.60	0.69
3	3166	979	502	0.86	0.76	0.81
4	1556	456	493	0.76	0.77	0.77
5	1713	243	760	0.69	0.88	0.77
6	210	98	120	0.64	0.68	0.66
7	440	102	405	0.52	0.81	0.63
8	3861	313	954	0.80	0.93	0.86
9	1322	580	611	0.68	0.70	0.69
TOTAL	**15323**	**4623**	**4711**	**0.76**	**0.77**	**0.77**

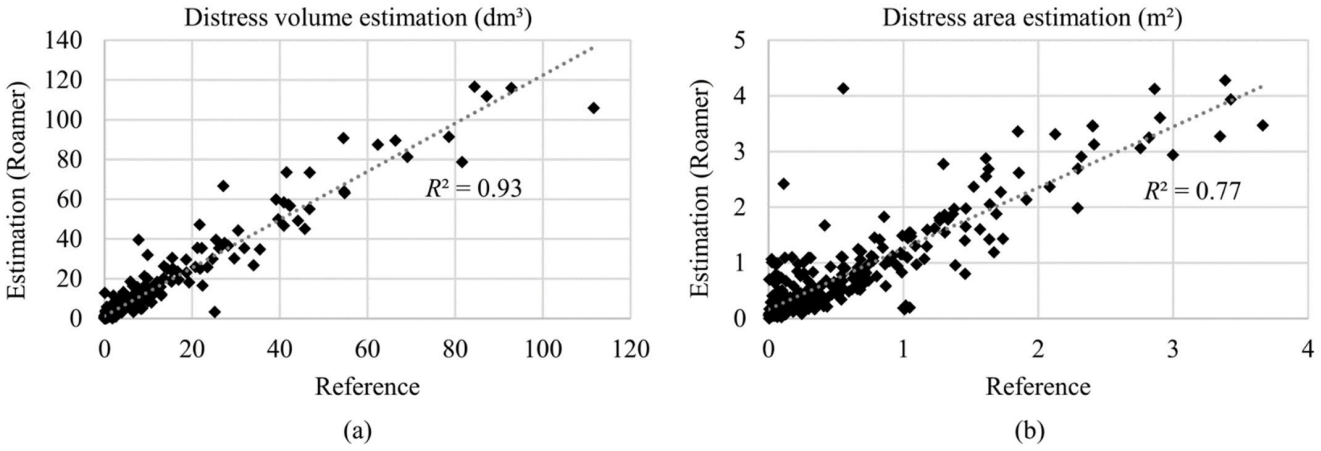

FIGURE 7. Scatter plots of distress volume (a) and area (b) estimates in the test sections. The grey dotted line represents a linear regression fit, illustrating the relationship between the estimates derived from Roamer data and the reference.

evaluation, the Roamer-based results achieved an F_1 score of 0.66. Correspondingly, recall and precision were 0.71 and 0.62, respectively. While the F_1 score was lower than that from the nine validation sections, the results still support robustness of the detection approach under more diverse and realistic conditions. The reduced accuracy in this larger dataset can be partly attributed to the nature of the reference data, which was generated automatically rather than through manual annotation. As described in Sections III-B and IV-A, the algorithm used to create the reference data achieved an F_1 score of 0.87, indicating it introduces some level of error. Consequently, comparisons against this reference likely underestimate the true performance of the algorithm, especially when compared to the manually annotated reference used in the earlier validation.

C. VOLUME AND AREA CALCULATION FOR PAVEMENT DISTRESSES

The evaluation of distress volume calculations across the 322 test sections showed a strong correlation of 0.96 and an R^2 of 0.93 between the Roamer and reference data (Fig. 7(a)). The RMSE was 7.21 dm^3, the MAE was 3.67 dm^3, and the bias was 3.16 dm^3. On average, the Roamer-based detection overestimated the distress volumes.

In comparison, when focusing on the distress area, the Roamer data showed a good correlation of 0.88 and an R^2 of 0.77 against the reference data. The metrics also showed an RMSE of 0.46 m^2, a MAE of 0.28 m^2, and a bias of 0.22 m^2. Similarly, the Roamer-based detection tended to overestimate the distress area. Results are visually presented in Fig. 7(b), where scatter plots and fitted regression lines illustrate the relationship between the estimation results from Roamer and reference data for both volume and area.

The lower R^2 value for area (0.77) compared to volume (0.93) is primarily due to the algorithm's dependence on geometric elevation differences. Small or shallow distresses, typically characterized by small elevation changes, are more likely to be missed or incompletely captured, which disproportionately affects area calculations. In contrast, volume calculations are less sensitive to the exclusion of points from these minor distresses or to false positives, since such points typically contribute very little to total volume due to their negligible depth. Therefore, despite some limitations in detecting low-severity features, the Roamer

TABLE 4. Volume and area calculation metrics between roamer and reference data.

	R^2	Correlation	RMSE	MAE	Bias
Volume	0.93	0.96	7.21 dm^3	3.67 dm^3	3.16 dm^3
Area	0.77	0.88	0.46 m^2	0.28 m^2	0.22 m^2

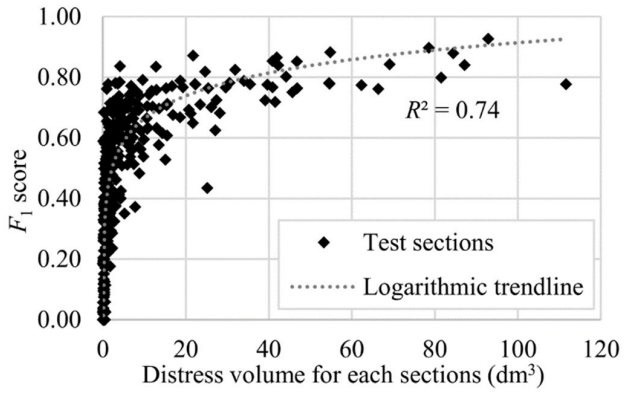

FIGURE 8. Relation between total distress volume in each test section from reference system and corresponding F_1 scores, showing a positive logarithmic trend.

system remains reliable, particularly for distress volume evaluations.

A summary of the results, including correlation, R^2 values, RMSE, MAE and bias for both volume and area calculations is shown in Table 4. The table consolidates the key metrics and highlights the consistent performance of the Roamer system across all test sections.

To better understand the factors influencing distress detection performance, further analysis was conducted to examine the relationship between distress volume and the F_1 score. Fig. 8 illustrates the relationship between the pavement distress detection F_1 score identified by Roamer data and the total volumes of distresses detected with the reference data in each test section, showing a positive logarithmic trend with an R^2 value of 0.74. This correlation highlights the improved performance of the algorithm as the distress volume increases.

As shown in Fig. 8, sections with lower total distress volumes tend to correspond with greater variability in F_1 scores, indicating the challenge of detecting shallow or low-severity distresses. This pattern further highlights the algorithm's limitations in handling minor elevation changes, which may also fall below the scanner's detection threshold or be filtered out during preprocessing. However, the overall performance confirms the system's reliability for volume estimation under practical road conditions.

D. FURTHER DISCUSSION ON DISTRESS ESTIMATION

The main objective of this study was to assess the capability of a conventional MLS system, such as Roamer-R4DW, to detect pavement distresses using a refined, novel algorithm. The results across validation and test sections demonstrated that, despite the limitations of conventional lower-resolution MLS data, the algorithm performed reliably in both distress detection and quantification tasks. The study also confirmed that high-quality reference data plays a crucial role in establishing accurate ground truth, which is essential for validating detection performance.

While the detection algorithm showed reliable performance, some challenges emerged in the evaluation process. One challenge involved the detection of shallow distresses during manual annotation. In the high-accuracy reference system, these features could still be identified using a combination of elevation and intensity information. However, due to their minimal elevation contrast, they were difficult to distinguish using geometric information alone. In addition to this technical limitation, a further challenge was the subjectivity involved in manually inspecting and labeling distress points, particularly at the boundaries of distresses. Inconsistencies in defining the exact edges can affect width and area measurements, which, in turn, influence evaluation metrics such as the F_1 score. This highlights the need for more objective and standardized annotation practices, possibly supported by semi-automated labeling tools or clearer visual guidelines.

One of the key considerations in designing detection systems for road maintenance is the trade-off between false positives and false negatives. Our two-out-of-three fusion strategy (Eq. 1) was selected to optimize for a balanced F_1 score, a common metric for algorithm benchmarking. While this approach increases precision, it can also raise the risk of false negatives, which may be problematic in safety-critical applications. However, it is important to note that because all three underlying algorithms are strongly relying on geometric features, this risk is mitigated for the most significant distress types. Structurally critical distresses, such as wide cracks and potholes, produce robust geometric signatures that are likely to be detected by at least two algorithms. Therefore, the false negatives introduced by the two-out-of-three system are more likely to be shallow, low-severity features rather than major structural faults. Furthermore, this decision-level framework is tunable without any architectural changes: a one-out-of-three configuration can be used to prioritize recall and minimize false negatives, while a three-out-of-three configuration can maximize precision. This flexibility allows the system to be adapted for different operational needs. Future research could explore more advanced decision-level fusion techniques, such as weighted voting or analyzing the precision-recall curve of the underlying algorithms to select the optimal detection balance.

The geometric parameters and voting logic of the proposed method also impose specific constraints on the detection of large-scale distresses. Specifically, the surface fitting algorithm utilizes a 50 × 50 cm fitting window; if a distress significantly exceeds this dimension, the reference surface may fit to the bottom of the distress. However, due to the overlapping processing strategy, adjacent windows inevitably span the distress boundary. Similarly, the surface roughness algorithm may classify a wide, flat distress bottom as

non-distress. Consequently, very large potholes (e.g., >50 cm in both horizontal directions) may result in a 'donut effect', where the boundaries are robustly detected by overlapping windows, but the center is missed. However, this study focused on paved roads where maintenance standards typically prevent such large failures; the possible limitation in detectable distress size is unlikely to affect overall detection accuracy. Moreover, future research could address this limitation using adaptive window sizing.

Similarly, distress detection at the lane boundary is challenged by the absence of adjacent pavement data beyond the lane edge for reference surface construction. While this study mitigated this using a 20 cm processing buffer, future applications could leverage the Roamer system's full 360-degree field of view to process the entire measurable pavement width for valid surface generation, subsequently clipping the results to the specific area of interest.

The edges of non-distress features, such as painted road markings or surface patches, were occasionally misidentified as distresses due to local elevation differences, further complicating the detection process. These issues underline the importance of refining the algorithm to better distinguish between true distress and surface artifacts, possibly by incorporating object-based classification approaches. However, this high sensitivity to minor elevation changes also presents a valuable opportunity: the same data could be leveraged to quantify the thickness and degradation of road markings, providing another key metric for maintenance planning.

The current limitations in point density and ranging accuracy of the Roamer system directly impact the reliable detection of small or shallow distresses, a key consideration for operational settings. The scanner's ranging accuracy of 5 mm with 3 mm precision means that shallow distresses may be obscured by the system's inherent measurement noise. If a distress feature's depth is in the same order as the scanner's accuracy, it becomes geometrically difficult for the algorithm to distinguish it from the non-distressed pavement surface. However, these features might still be identifiable using the scanner's intensity data.

Furthermore, the along-track profile spacing of 4–5 cm in the Roamer system, dependent on driving speed, poses a significant challenge for detecting narrow distresses. Narrow transverse cracks can be missed entirely if they happen to fall between consecutive scan profiles. This limitation is implicitly acknowledged in our evaluation (Table 3), which focused on distresses wider than 2 cm, as the detection of narrower features is inherently unreliable with this system configuration. These limitations underline that while the Roamer system is effective for more significant pavement distresses, its operational use requires accepting a lower detection rate for fine-scale distresses. Future improvements, such as the adoption of dual-scanner setups or next-generation LiDAR systems, would directly address these challenges by significantly improving point coverage and geometric precision, enabling more accurate and comprehensive pavement condition assessments.

Pavement distresses directly influence driving comfort and safety. Accurate detection of such distresses is fundamental for reliable pavement condition evaluation and further maintenance planning. This study specifically focuses on the detection and accuracy assessment of pavement distresses using 3D point cloud data, rather than a comprehensive pavement condition evaluation, which would typically involve assessing damage type, severity, or analyzing its causes. The proposed method and system enable precise identification and characterization of pavement distresses, providing essential quantitative indicators (e.g., volume, area, depth and width) for subsequent condition assessment and management. Future work should integrate these detected distress metrics into comprehensive pavement condition assessments. This is crucial, as each country maintains its own standards for detailed damage assessment and subsequent road maintenance protocols.

V. CONCLUSION

This study quantitatively evaluated the capability of a conventional MLS system, capable of mapping both the road surface and surrounding environment in 3D, for pavement distress detection. The evaluation followed a three-stage approach: algorithm validation using high-accuracy PPS-plus data, performance testing on conventional MLS system data, and a larger-scale generalization analysis. The focus was on both detection accuracy and the estimation of distress volume and area.

The algorithm, refined from previous work [22] demonstrated strong performance when it was validated on PPS-plus data. When applied to nine manually annotated 10-meter-long validation sections, the algorithm achieved an F_1 score of 0.87, with precision and recall values of 0.87 each for detecting distresses wider than 2 cm. In an additional test, the algorithm was evaluated on detecting all distresses wider than 1 cm and maintained high performance, achieving an F_1 score of 0.85.

We then applied the validated algorithm to data acquired by a conventional Roamer MLS system and compared the outputs to the same high-accuracy manual reference used in the PPS-plus evaluation. Despite the lower point density and ranging precision of the Roamer system, the algorithm achieved an F_1 score of 0.77 (precision 0.77, recall 0.76), demonstrating solid performance across all nine 10-meter-long validation sections.

To assess generalizability, we extended the evaluation to a 3.2-km road segment divided into 322 10-meter-long test sections. In this larger-scale comparison, where the reference was algorithm-generated from PPS-plus data, the Roamer system achieved an F_1 score of 0.66, with a recall of 0.71 and precision of 0.62.

In addition to detection accuracy, we evaluated the Roamer system's ability to estimate distress volume and area. The R^2 was 0.93 for volume and 0.77 for area, indicating a high level of consistency with the reference data. For volume, the RMSE, MAE, and bias were 7.21 dm^3, 3.67 dm^3, and

3.16 dm^3, respectively. For area, the RMSE was 0.46 m^2, the MAE was 0.28 m^2, and the bias was 0.22 m^2.

These findings confirm the effectiveness of the proposed algorithm and demonstrate the capability of conventional MLS systems, such as the Roamer-R4DW, to reliably detect and quantify pavement distress, even when operating at a lower resolution compared to high-accuracy reference systems. As MLS systems continue to evolve and become more accessible, the ability to detect smaller distresses will improve, supporting broader applications in data-driven road infrastructure monitoring. The results of this study emphasize the evolving nature of MLS-based distress detection and point to a future where technological improvements and methodological refinements converge to enable more accurate and efficient pavement evaluations as part of the full road environment mapping.

DATA AVAILABILITY

The representative datasets supporting the findings of this study are available in the Zenodo repository at https://doi.org/10.5281/zenodo.19267189 [44].

AUTHOR CONTRIBUTION

Aimad El Issaoui was responsible for method development, developing the original surface fitting algorithm, improving the profile-based filtering and local surface roughness algorithms, creating the combined distress detection algorithm, developing the method for ideal profile fitting and distress volume/area calculation, performing statistical analysis, preparing the field test, registering the point cloud data, writing and reviewing the manuscript, and contributed to Roamer data collection and the lane extraction process. Ziyi Feng was responsible for developing the original profile-based filtering algorithm and the noise removal method, and contributed to method development, data quality analysis, writing, and reviewing. Matti Lehtomäki was responsible for developing the original surface roughness algorithm and lane extraction, and contributed to road marking extraction, statistical analysis, writing, and reviewing. Josef Taher contributed to statistical analysis and reviewing. Harri Kaartinen and Antero Kukko were responsible for the study design and supervision, and contributed to the data collection and preprocessing of Roamer data, statistical analysis, and reviewing. Daniel Steiger and Alexander Reiterer were responsible for the data collection and preprocessing of PPS data, and contributed to reviewing. Hannu Hyyppä was co-PI of the project, responsible for the Aalto share of the consortium in both Research Council of Finland and European Regional Development Fund and Uudenmaan liitto funding. Juha Hyyppä was the senior author and PI of the work, acquired the listed funding, supervised the work, developed the concept with Aimad El Issaoui, and contributed in reviewing and improving the manuscript.

ACKNOWLEDGMENT

(Aimad El Issaoui and Ziyi Feng are co-first authors.)

REFERENCES

[1] M. G. Arab, M. Alzara, W. Zeiada, M. Omar, and A. Azam, "Combined effect of compaction level and matric suction conditions on flexible pavement performance using construction and demolition waste," *Construct. Building Mater.*, vol. 261, Nov. 2020, Art. no. 119792, doi: 10.1016/j.conbuildmat.2020.119792.

[2] E. Mousa, S. El-Badawy, and A. Azam, "Effect of reclaimed asphalt pavement in granular base layers on predicted pavement performance in Egypt," *Innov. Infrastruct. Solutions*, vol. 5, no. 2, p. 57, Aug. 2020, doi: 10.1007/s41062-020-00301-2.

[3] N. Baldo, M. Miani, F. Rondinella, J. Valentin, P. Vackcová, and E. Manthos, "Stiffness data of high-modulus asphalt concretes for road pavements: Predictive modeling by machine-learning," *Coatings*, vol. 12, no. 1, p. 54, Jan. 2022, doi: 10.3390/coatings12010054.

[4] Y. Ge, J. Liu, X. Zhang, H. Tang, and X. Xia, "Automated detection and characterization of cracks on concrete using laser scanning," *J. Infrastructure Syst.*, vol. 29, no. 2, Jun. 2023, Art. no. 04023005, doi: 10.1061/jitse4.iseng-1936.

[5] R. Napolitano and B. Glisic, "Methodology for diagnosing crack patterns in masonry structures using photogrammetry and distinct element modeling," *Eng. Struct.*, vol. 181, pp. 519–528, Feb. 2019, doi: 10.1016/j.engstruct.2018.12.036.

[6] Y.-C.-J. Tsai and F. Li, "Critical assessment of detecting asphalt pavement cracks under different lighting and low intensity contrast conditions using emerging 3D laser technology," *J. Transp. Eng.*, vol. 138, no. 5, pp. 649–656, May 2012, doi: 10.1061/(asce)te.1943-5436.0000353.

[7] Y. Hu and C.-X. Zhao, "A novel LBP based methods for pavement crack detection," *J. Pattern Recognit. Res.*, vol. 5, no. 1, pp. 140–147, 2010, doi: 10.13176/11.167.

[8] Q. Zou, Y. Cao, Q. Li, Q. Mao, and S. Wang, "CrackTree: Automatic crack detection from pavement images," *Pattern Recognit. Lett.*, vol. 33, no. 3, pp. 227–238, Feb. 2012, doi: 10.1016/j.patrec.2011.11.004.

[9] M. Salman, S. Mathavan, K. Kamal, and M. Rahman, "Pavement crack detection using the Gabor filter," in *Proc. 16th Int. IEEE Conf. Intell. Transp. Syst. (ITSC)*, Oct. 2013, pp. 2039–2044, doi: 10.1109/ITSC.2013.6728529.

[10] H. Guan et al., "Iterative tensor voting for pavement crack extraction using mobile laser scanning data," *IEEE Trans. Geosci. Remote Sens.*, vol. 53, no. 3, pp. 1527–1537, Mar. 2015, doi: 10.1109/TGRS.2014.2344714.

[11] S. Varadharajan, S. Jose, K. Sharma, L. Wander, and C. Mertz, "Vision for road inspection," in *Proc. IEEE Winter Conf. Appl. Comput. Vis.*, Mar. 2014, pp. 115–122, doi: 10.1109/WACV.2014.6836111.

[12] Y. Shi, L. Cui, Z. Qi, F. Meng, and Z. Chen, "Automatic road crack detection using random structured forests," *IEEE Trans. Intell. Transp. Syst.*, vol. 17, no. 12, pp. 3434–3445, Dec. 2016, doi: 10.1109/TITS.2016.2552248.

[13] L. Zhang, F. Yang, Y. Daniel Zhang, and Y. J. Zhu, "Road crack detection using deep convolutional neural network," in *Proc. IEEE Int. Conf. Image Process. (ICIP)*, Phoenix, AZ, USA, Sep. 2016, pp. 3708–3712, doi: 10.1109/ICIP.2016.7533052.

[14] R. Fan et al., "Road crack detection using deep convolutional neural network and adaptive thresholding," in *Proc. IEEE Intell. Vehicles Symp. (IV)*, Jun. 2019, pp. 474–479, doi: 10.1109/IVS.2019.8814000.

[15] R. Jiang, D. V. Jáuregui, and K. R. White, "Close-range photogrammetry applications in bridge measurement: Literature review," *Measurement*, vol. 41, no. 8, pp. 823–834, Oct. 2008, doi: 10.1016/j.measurement.2007.12.005.

[16] E. Salari and G. Bao, "Automated pavement distress inspection based on 2D and 3D information," in *Proc. IEEE Int. Conf. Electro/Inf. Technol.*, May 2011, pp. 1–4, doi: 10.1109/EIT.2011.5978575.

[17] M. Weinmann, B. Jutzi, and C. Mallet, "Feature relevance assessment for the semantic interpretation of 3D point cloud data," *ISPRS Ann. Photogramm., Remote Sens. Spatial Inf. Sci.*, vol. 5, pp. 313–318, Oct. 2013, doi: 10.5194/isprsannals-ii-5-w2-313-2013.

[18] Q. Hu et al., "RandLA-Net: Efficient semantic segmentation of large-scale point clouds," in *Proc. IEEE/CVF Conf. Comput. Vis. Pattern Recognit. (CVPR)*, Jun. 2020, pp. 11105–11114, doi: 10.1109/CVPR42600.2020.01112.

[19] A. Zhang et al., "Automated pixel-level pavement crack detection on 3D asphalt surfaces with a recurrent neural network," *Comput.-Aided Civil Infrastruct. Eng.*, vol. 34, no. 3, pp. 213–229, Mar. 2019, doi: 10.1111/mice.12409.

[20] G. Bitelli, A. Simone, F. Girardi, and C. Lantieri, "Laser scanning on road pavements: A new approach for characterizing surface texture," *Sensors*, vol. 12, no. 7, pp. 9110–9128, Jul. 2012, doi: 10.3390/s120709110.

[21] A. El Issaoui et al., "Feasibility of mobile laser scanning towards operational accurate road rut depth measurements," *Sensors*, vol. 21, no. 4, p. 1180, Feb. 2021, doi: 10.3390/s21041180.

[22] Z. Feng et al., "Pavement distress detection using terrestrial laser scanning point clouds – accuracy evaluation and algorithm comparison," *ISPRS Open J. Photogramm. Remote Sens.*, vol. 3, Jan. 2022, Art. no. 100010, doi: 10.1016/j.ophoto.2021.100010.

[23] Y.-C.-J. Tsai and A. Chatterjee, "Pothole detection and classification using 3D technology and watershed method," *J. Comput. Civil Eng.*, vol. 32, no. 2, Mar. 2018, Art. no. 04017078, doi: 10.1061/(asce)cp.1943-5487.0000726.

[24] M. R. De Blasiis, A. Di Benedetto, and M. Fiani, "Mobile laser scanning data for the evaluation of pavement surface distress," *Remote Sens.*, vol. 12, no. 6, p. 942, Mar. 2020, doi: 10.3390/rs12060942.

[25] Y. Tsai and Z. Yang, "New pavement performance indicators using crack fundamental elements and 3D pavement surface data with multiple-timestamp registration for crack deterioration analysis and optimal treatment determination," *Transp. Res. Rec., J. Transp. Res. Board*, vol. 2674, no. 7, pp. 115–126, Jul. 2020, doi: 10.1177/0361198120920877.

[26] R. Ravi, D. Bullock, and A. Habib, "Pavement distress and debris detection using a mobile mapping system with 2D profiler LiDAR," *Transp. Res. Rec., J. Transp. Res. Board*, vol. 2675, no. 9, pp. 428–438, Sep. 2021, doi: 10.1177/03611981211002529.

[27] Z. Yang, X. Zhang, Y. Tsai, and Z. Wang, "Quantitative assessments of crack sealing benefits by 3D laser technology," *Transp. Res. Rec., J. Transp. Res. Board*, vol. 2675, no. 12, pp. 103–116, Dec. 2021, doi: 10.1177/03611981211027897.

[28] P. del Río-Barral, M. Soilán, S. M. González-Collazo, and P. Arias, "Pavement crack detection and clustering via region-growing algorithm from 3D MLS point clouds," *Remote Sens.*, vol. 14, no. 22, p. 5866, Nov. 2022, doi: 10.3390/rs14225866.

[29] B. Al-Mistarehi, A. Shtayat, R. Imam, and A. Abdallah, "An automated assessment technique for pavement defects using a laser scanner and deep machine learning," *Civil Eng. J.*, vol. 11, no. 3, pp. 1088–1105, Mar. 2025, doi: 10.28991/cej-2025-011-03-015.

[30] Y. Zhang et al., "A Kinect-based approach for 3D pavement surface reconstruction and cracking recognition," *IEEE Trans. Intell. Transp. Syst.*, vol. 19, no. 12, pp. 3935–3946, Dec. 2018, doi: 10.1109/TITS.2018.2791476.

[31] H. Feng et al., "GCN-based pavement crack detection using mobile LiDAR point clouds," *IEEE Trans. Intell. Transp. Syst.*, vol. 23, no. 8, pp. 11052–11061, Aug. 2022, doi: 10.1109/TITS.2021.3099023.

[32] L. Yan, H. Liu, J. Tan, Z. Li, H. Xie, and C. Chen, "Scan line based road marking extraction from mobile LiDAR point clouds," *Sensors*, vol. 16, no. 6, p. 903, Jun. 2016, doi: 10.3390/s16060903.

[33] M. Zhong, L. Sui, Z. Wang, and D. Hu, "Pavement crack detection from mobile laser scanning point clouds using a time grid," *Sensors*, vol. 20, no. 15, p. 4198, Jul. 2020, doi: 10.3390/s20154198.

[34] P. del Río-Barral, J. Grandío, B. Riveiro, and P. Arias, "Identification of relevant point cloud geometric features for the detection of pavement cracks using MLS data," *Int. Arch. Photogramm., Remote Sens. Spatial Inf. Sci.*, vol. 1, pp. 107–112, May 2023, doi: 10.5194/isprs-archives-xlviii-1-w1-2023-107-2023.

[35] M. Guo et al., "Intelligent extraction of road cracks based on vehicle laser point cloud and panoramic sequence images," *J. Road Eng.*, vol. 4, no. 1, pp. 69–79, Mar. 2024, doi: 10.1016/j.jreng.2024.01.004.

[36] M. Xia, X. Qin, Q. Mao, G. Jing, J. Zhu, and Y. Shi, "Subsidence detection of asphalt pavement based on mobile laser scanning system," *IEEE Sensors J.*, vol. 24, no. 20, pp. 33148–33159, Oct. 2024, doi: 10.1109/JSEN.2024.3450723.

[37] N. Pascucci, D. Dominici, and A. Habib, "LiDAR-based road cracking detection: Machine learning comparison, intensity normalization, and open-source WebGIS for infrastructure maintenance," *Remote Sens.*, vol. 17, no. 9, p. 1543, Apr. 2025, doi: 10.3390/rs17091543.

[38] Fraunhofer IPM. (2024). *Pavement Profile Scanner PPS*. Accessed: Jun. 16, 2025. [Online]. Available: https://www.ipm.fraunhofer.de/content/dam/ipm/en/PDFs/product-information/OF/MTS/Pavement-Profile-Scanner-PPS.pdf

[39] T. Lundberg, P. Andrén, T. Wahlman, and O. Eriksson, "New technology for road surface measurement," Swedish Nat. Road Transp. Res. Inst. (VTI), Linköping, Sweden, Tech. Rep. VTI Report 961A, 2018.

[40] Z. Pan et al., "One-stage 3D profile-based pavement crack detection and quantification," *Autom. Construction*, vol. 153, Sep. 2023, Art. no. 104946, doi: 10.1016/j.autcon.2023.104946.

[41] Y. Du et al., "A pothole detection method based on 3D point cloud segmentation," in *Proc. 12th Int. Conf. Digit. Image Process. (ICDIP)*. Bellingham, WA, USA: SPIE, Jun. 2020, p. 54, doi: 10.1117/12.2573124.

[42] R. Fan, U. Ozgunalp, B. Hosking, M. Liu, and I. Pitas, "Pothole detection based on disparity transformation and road surface modeling," *IEEE Trans. Image Process.*, vol. 29, pp. 897–908, 2020, doi: 10.1109/TIP.2019.2933750.

[43] (2024). *CloudCompare*. Accessed: Jan. 26, 2025. [Online]. Available: https://www.cloudcompare.org

[44] A. El Issaoui et al., "Mobile laser scanning for road pavement distress detection, dataset," Zenodo, Geneva, Switzerland, Tech. Rep., 2026, doi: 10.5281/zenodo.19267189.